JCI insight

RESEARCH ARTICLE

Injury-induced actin cytoskeleton reorganization in podocytes revealed by super-resolution microscopy

Hani Y. Suleiman,[1] Robyn Roth,[2] Sanjay Jain,[1] John E. Heuser,[3] Andrey S. Shaw,[4] and Jeffrey H. Miner[1]

[1]Division of Nephrology, Department of Medicine, Washington University School of Medicine, St. Louis, Missouri, USA. [2]Washington University Center for Cellular Imaging, Washington University School of Medicine, St. Louis, Missouri, USA. [3]Institute for Integrated Cell-Material Sciences (iCeMS), Kyoto University, Kyoto, Japan. [4]Genentech, South San Francisco, California, USA.

The architectural integrity of tissues requires complex interactions, both between cells and between cells and the extracellular matrix. Fundamental to cell and tissue homeostasis are the specific mechanical forces conveyed by the actomyosin cytoskeleton. Here we used super-resolution imaging methods to visualize the actin cytoskeleton in the kidney glomerulus, an organized collection of capillaries that filters the blood to make the primary urine. Our analysis of both mouse and human glomeruli reveals a network of myosin IIA–containing contractile actin cables within podocyte cell bodies and major processes at the outer aspects of the glomerular tuft. These likely exert force on an underlying network of myosin IIA–negative, noncontractile actin fibers present within podocyte foot processes that function to both anchor the cells to the glomerular basement membrane and stabilize the slit diaphragm against the pressure of fluid flow. After injuries that disrupt the kidney filtration barrier and cause foot process effacement, the podocyte's contractile actomyosin network relocates to the basolateral surface of the cell, manifesting as sarcomere-like structures juxtaposed to the basement membrane. Our findings suggest a new model of the podocyte actin cytoskeleton in health and disease and suggest the existence of novel mechanisms that regulate podocyte architecture.

Introduction

The actin cytoskeleton is an important mediator of cell shape, traction force generation, and cell motility. Although actin and nonmuscle myosin IIA can be detected in the majority of cells in all tissues, in most cases other than muscle cells, actin is not found in a filamentous pattern, but rather in an amorphous pattern. It has been suggested that filamentous actin in the form of long, thick, contractile stress fibers may be an artifact of in vitro culture stimulated by the attachment of cells to rigid substrates, such as plastic or glass. However, there are a few examples of cells with prominent stress fibers in vivo, including cells involved in the closure of epithelial sheets during embryogenesis, myoepithelial cells in wounds (1, 2) and in mammary glands (3), and endothelial cells of large blood vessels (4–6). A common feature is the high level of mechanical stress experienced by cells with stress fibers.

Cells can be identified as either stationary or motile in terms of the use of their stress fibers (7). Highly contractile cells such as muscle, ductal, and tubular cells are less likely to be motile and instead are thought to apply force to their surroundings. Cultured cells generate isometric tension and stress fibers as a result of interactions with their surrounding environment, such as a rigid extracellular matrix (8, 9). Aside from stress fibers, cultured cells can generate 2 other types of structures by altering their actin cytoskeleton: lamellepodia, broad cellular protrusions with dendritic actin mats; and filopodia, slender cellular protrusions with bundled actin filaments (10). A variety of actin-binding proteins regulates the size, shape, stability and resilience of actin structures (11). Dynamic contractile forces play critical roles in organogenesis and cell migration (12).

In cultured fibroblasts, 3 types of actin stress fibers have been described. Noncontractile dorsal stress fibers (DSFs), thought to serve as mechanosensors, are connected to a focal adhesion on one end and

Conflict of interest: J.H. Miner has received licensing fees from Genentech and Eli Lilly, research funding from F. Hoffmann-La Roche, and advisory board income from Regulus Therapeutics.

Submitted: May 17, 2017
Accepted: July 7, 2017
Published: August 17, 2017

Reference information:
JCI Insight. 2017;2(16):e94137. https://doi.org/10.1172/jci.insight.94137.

extend apically towards the inside of the cell (13, 14). DSFs are connected to long curved contractile fibers called transverse arcs (TAs) that extend around the circumference of the cell. Lastly, contractile ventral stress fibers (VSFs) run parallel to the substrate and connect 2 focal adhesions to each other. VSFs may represent TAs that have moved down from the apical side of the cell to the ventral surface (7, 15). As contractile fibers, TAs and VSFs are characterized by a sarcomere-like pattern with alternating localization of α-actinin and myosin II on the actin filament.

The glomerulus is a bed of capillary loops that filters the blood. Glomerular endothelial cells line the inner wall of the capillary, and epithelial podocytes cover the outer wall. These 2 cell types spread on and adhere to the glomerular basement membrane (GBM) that lies between them (16). The podocytes play a unique role; they provide structural support against the hydrodynamic pressures of vascular flow as well as establish slit diaphragms, specialized cell-cell contacts that allow filtrate to pass between the foot processes. In addition, podocytes must achieve an elasticity that allows the capillary to expand and contract with each heartbeat.

The special properties of the podocyte are likely mediated by its unique cytoskeletal structure. While microtubules and intermediate filaments are largely present in the cell body and the major processes, foot processes are thought to contain only an elaborate actin network (17). The interaction between actin fibers and myosin motor proteins plays a critical role in generating mechanical stress, allowing for distinct cell shapes. Exactly how the actomyosin network is organized in podocytes is not known (17–19).

The importance of the podocyte actin cytoskeleton is demonstrated by the fact that genetic forms of glomerular disease are often caused by mutations that affect proteins associated with it (20). Podocyte injury leads to a change in podocyte morphology such that foot processes are reduced in frequency or can no longer be distinguished, which is called foot process effacement (FPE). FPE results in an impairment of the filtration barrier with leakage of plasma proteins such as albumin into the urine. Morphologically, FPE is characterized by loss or widening of the interdigitated foot processes, resulting in a broad flattened cell projection that covers the GBM. In many cases FPE is accompanied by the appearance of an actin mat juxtaposed to the GBM (21, 22) and observed after both human and animal podocyte injuries (23). A dynamic disruption of the actin cytoskeleton leads to a profound disruption of the filtration barrier (24).

Imaging actin filaments in tissue is hampered by their small size and the fact that most tissue fixation methods result in their destabilization (25). Here we used a variety of methods to resolve how actin, myosin, and the actin-binding proteins α-actinin-4 and synaptopodin are organized in whole glomeruli. Our work demonstrates a complex network of contractile and noncontractile actin cables that likely function to stabilize the capillary against the hydrostatic pressures of the blood. In addition, our work details molecular changes in the cytoskeleton that occur after podocyte injury and disruption of the filtration barrier in 3 different injury models. Our results provide potentially novel insights into the distribution of cytoskeletal proteins and suggest novel mechanisms for their involvement in FPE.

Results

Super-resolution imaging of podocyte foot processes. Podocyte foot processes are 200–300 nm in width, while the slit diaphragms that separate and connect them are around 30–40 nm. Because the resolution of the light microscope is limited to 200–400 nm, podocyte foot processes and slit diaphragms cannot be imaged analytically by traditional light microscopy; instead, electron microscopy is the method of choice. To determine whether the stochastic optical reconstruction microscopy (STORM; see ref. 26) super-resolution microscopy approach could be used to image foot processes and slit diaphragms, we stained ultrathin kidney sections with antibodies against the extracellular domain of nephrin, a component of the slit diaphragm. To orient the localization of nephrin relative to the GBM, we costained for agrin, which localizes to the subepithelial and subendothelial borders of the GBM (27). The nephrin antibody stained adjacent to the GBM in a clustered periodic pattern, with an average distance of 200–300 nm between clusters (Figure 1). Antibodies against podocin and CD2AP showed similar patterns of periodic clusters adjacent to the GBM (Figure 1, B and C).

Electron microscopy has shown that podocyte foot processes have a central actin bundle containing synaptopodin (28). By STORM, synaptopodin exhibited a clustered localization pattern distinct from nephrin, CD2AP, and podocin. Costaining for synaptopodin and nephrin helped to localize synaptopodin centrally within foot processes, between the slit diaphragms (Figure 1D). In most examples, synaptopodin clusters were linear and extended perpendicularly away from the GBM. A similar pattern was observed

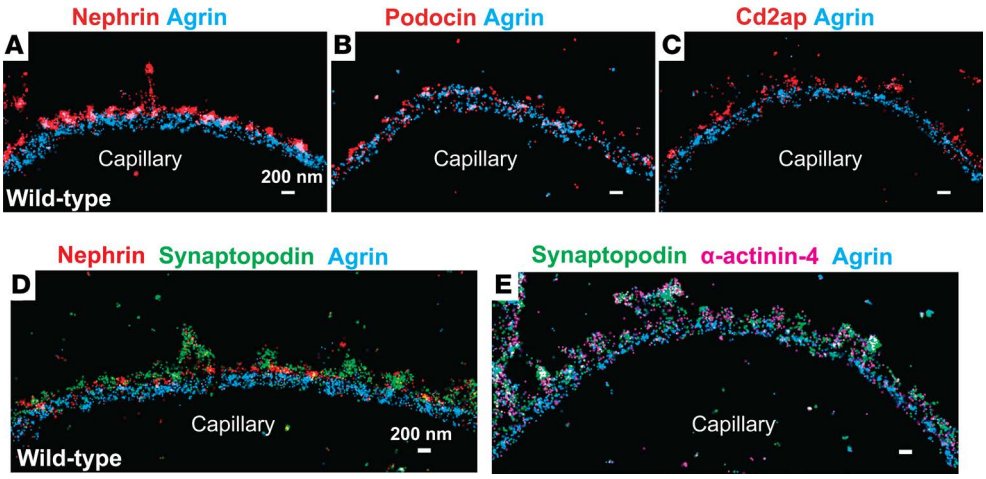

Figure 1. STORM imaging of slit diaphragm proteins. (**A**–**C**) Double-color STORM imaging of the glomerular basement membrane (GBM) protein agrin (blue) and slit diaphragm proteins nephrin (**A**, red), podocin (**B**, red), and CD2AP (**C**, red) showing how these proteins cluster near the subpodocyte aspect of the agrin-stained GBM. (**D**) Triple-color STORM imaging of agrin (blue), nephrin (red), and synaptopodin (green) shows that synaptopodin clusters are located between the individual nephrin clusters. (**E**) Triple-color STORM imaging of agrin (blue), synaptopodin (green), and α-actinin-4 (magenta) shows that synaptopodin and α-actinin-4 clusters colocalize. Scale bars: 200 nm.

using an antibody against α-actinin-4 (Figure 1E). This suggests that synaptopodin and α-actinin-4 are contained within the thick actin cable in the center of the foot process. We also detected focal clusters of α-actinin-4 (data not shown) and synaptopodin along the apical podocyte plasma membrane (Figure 2, A and B, arrowheads), suggesting the presence of circumferential actin filaments near the apical plasma membrane, as reported in cultured podocytes (29).

Change in myosin IIA localization after podocyte injury. Recently, it was shown that synaptopodin is mechanoresponsive, as it requires tension generated by myosin IIA for its proper function (30). Both contractile and noncontractile actin fibers are present in all cells; contractile fibers can be identified by the alternating localization of α-actinin and myosin along the actin fiber (31). To study the relationship between synaptopodin and contractile actin fibers in podocytes, we costained for synaptopodin and myosin IIA (Figure 2, A–C). To our surprise, in WT podocytes myosin IIA was not detected in the foot processes (distal) but rather was mainly found in the cell body and major processes (proximal) (Figure 2B, arrows). This suggested that the actin filaments in the foot processes are not contractile, whereas those in the cell body and major processes are contractile. We also detected myosin IIA in focal clusters along the apical podocyte plasma membrane (Figure 2B). This suggested that the membrane-associated circumferential actin filaments are contractile and likely the in vivo correlate to TA actin fibers that were only recently identified in cultured cells (15, 32, 33). Using an antibody against the other myosin II isoform, myosin IIB, we were unable to detect expression in podocytes, whereas mesangial cells were clearly myosin IIB positive, confirming earlier findings (Supplemental Figure 1; supplemental material available online with this article; https://doi.org/10.1172/jci.insight.94137DS1) (34).

To validate this finding, we sought a method to directly localize the molecular components of contractile actin fibers in whole glomeruli. For technical reasons, however, it is difficult to visualize actin fibers and cables in fixed tissue using fluorescent staining methods. The diameter of individual actin fibrils is below the resolution of light microscopy, and traditional fixation methods often result in destabilization of actin structures (25). More importantly, clear visualization of actin cables by light microscopy is hampered by the need to cut tissue sections, which transects most of the cables. We therefore developed methods to preserve actin cytoskeletal structures during and after fixation and to image glomeruli without the need for sectioning. Glomeruli were isolated using magnetic beads, and then membranes were extracted using a detergent solution containing phalloidin and taxol to preserve cytoskeletal structures. This was followed by paraformaldehyde fixation in the same buffer. Antibody staining was then performed in whole glomeruli, after which the glomeruli were mounted on glass slides and imaged by confocal microscopy.

Confocal images of encapsulated glomeruli stained with phalloidin and for myosin IIA revealed a wide network of thick myosin IIA–positive actin cables radiating across the surface of the glomerulus (Figure

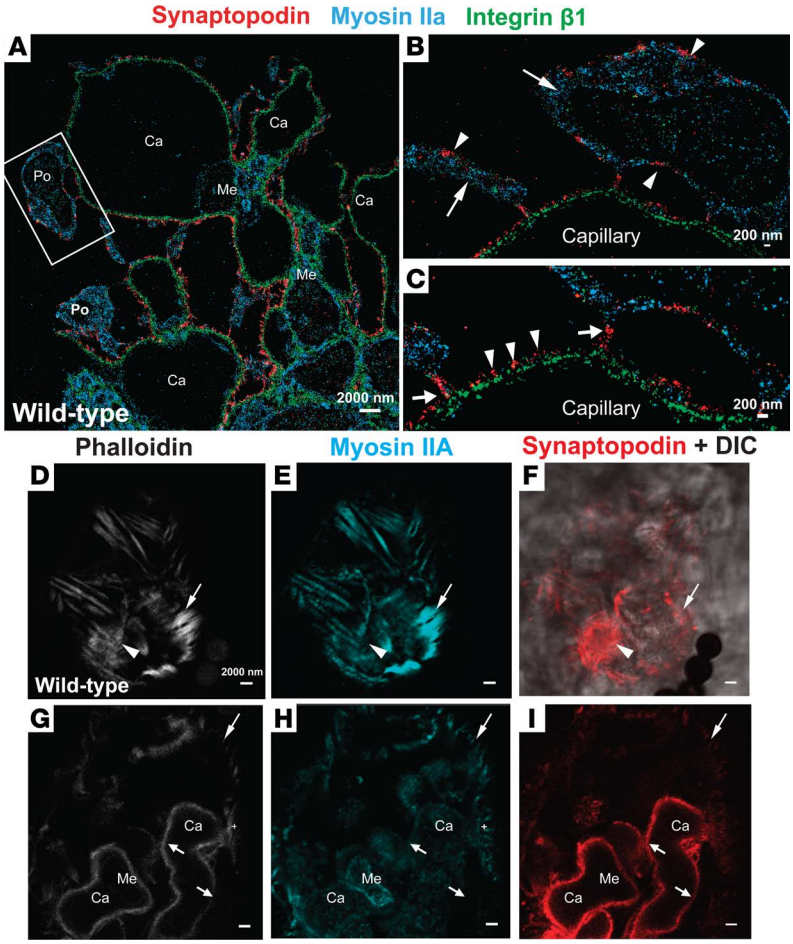

Figure 2. STORM imaging of myosin IIA's distribution in podocytes in healthy and diseased conditions. (**A**) Triple-color STORM overview image of a WT glomerulus shows myosin IIA's (blue) absence from foot processes in comparison with synaptopodin (red) and integrin β1 (green) labeling along the capillary wall. (**B** and **C**) Higher magnification images of the boxed area in **A** show that myosin IIA is present in the podocyte cell body and the primary processes (arrows in **B**) but not in the foot processes that contain synaptopodin (arrowheads in **C**). Note the transition between the foot processes and the primary processes (arrows in **C**). Synaptopodin patches were observed at the periphery of the podocyte cell body and primary processes (arrowheads in **B**). (**D**–**I**) Staining for actin (**D** and **G**), myosin IIA (**E** and **H**), and synaptopodin (**F** and **I**). (**D**–**F**) Confocal slices of the glomerular surface show the podocytes' thick actin cables positive for myosin IIA and negative for synaptopodin (arrows). Note the diffracted en face image of the capillary wall stained positive for actin and synaptopodin and very little myosin IIA (arrowheads). The differential interference contrast (DIC) overlay image (**F**) shows the shadow of magnetic beads (4 μm) used to isolate glomeruli. (**G**–**I**) Deep confocal imaging shows the capillary wall (small arrows) positive for phalloidin (**G**) and synaptopodin (**I**) but negative for myosin IIA (**H**). Note the myosin IIA–positive mesangial cell inside the capillary borders (**H**). Scale bars: 200 nm (**A**–**C**) and 2,000 nm (**D**–**I**). Ca, capillary; Me, mesangial cell.

2, D–F, and Supplemental Movie 1). These were mostly synaptopodin negative (Figure 2F). We confirmed that these cables belonged to podocytes by costaining with the podocyte marker WT1, which showed that the actin cables were contained within surface-exposed, WT1-positive cell bodies (Supplemental Figure 2). Deeper optical sections showed that in cross-sectional images of the capillary, thinner myosin IIA–negative noncontractile actin filaments were located near the capillary wall, presumably within foot processes, as they contained synaptopodin; the larger contractile filaments were distal and separated from the capillary wall (Figure 2, D–H).

Super-resolution imaging of normal and injured podocytes. To study the molecular changes that occur in podocytes after injury, and because the effects of injury can be heterogeneous, we correlated STORM images with electron microscopic images (STORM-EM correlation) using a freeze-etch EM method that we described previously (27). In WT podocytes, EM images of the areas stained for nephrin and agrin by STORM showed intact foot processes juxtaposed to the GBM (Figure 3, A–C). Higher magnification of these areas confirmed that nephrin clusters were located between individual foot processes, as they represent slit diaphragms just above the GBM (Figure 3, D–F).

When podocytes are injured in proteinuric kidney diseases, slit diaphragms are lost and foot processes change their morphology in association with FPE. To determine the fate of slit diaphragm proteins after injury, we used 3 mouse models of FPE. Two of the models, *Cd2ap*-KO and laminin β2 (*Lamb2*)–KO, are genetic models in which FPE begins during the second postnatal week (35, 36). In the third model, Adriamycin nephropathy, FPE occurs after an acute drug-induced injury (37). We first examined nephrin localization after injury. In all 3 models, STORM imaging showed loss of nephrin clusters near the GBM. Instead, the nephrin was diffusely distributed in the cytoplasm, mostly away from the GBM. STORM-EM correlation confirmed FPE and showed that nephrin had translocated to the apical surface of the podocyte and to large clusters inside the cell (Figure 3, G–I and J–L, and Supplemental Figures 3 and 4).

The slit diaphragm–associated proteins podocin and CD2AP localize differently after FPE. Genetic and cell

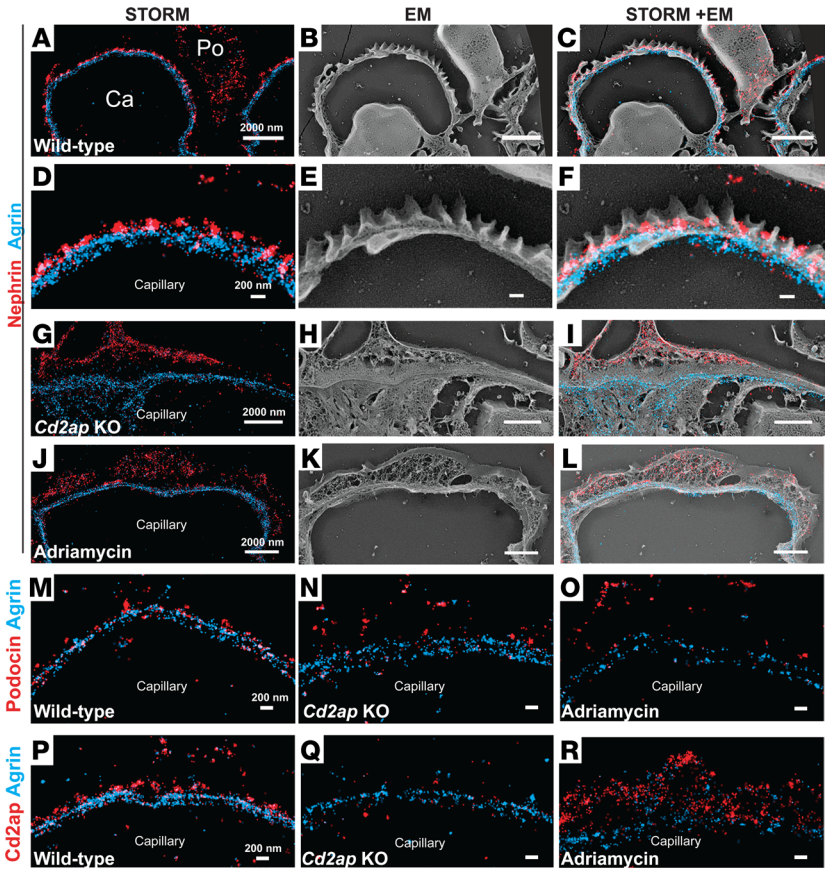

Figure 3. STORM and STORM-EM correlative imaging of slit diaphragm molecules in healthy and injured podocytes. (**A**–**F**) Double-color STORM imaging of nephrin and agrin with EM correlation. (**A**) Low and (**D**) high magnification images show nephrin clusters in a periodic pattern (red) adjacent to the glomerular basement membrane (GBM) labeled with agrin (blue). (**B** and **E**) Deep-etch freeze fracture (DEFF) EM images of the same areas in **A** and **D** show individual foot processes on the capillary wall. (**C** and **F**) STORM-EM correlation shows that nephrin staining is between individual foot processes. (**G**–**L**) STORM (**G** and **J**), DEFF-EM (**H** and **K**), and STORM-EM correlation images of capillary walls of *Cd2ap*-KO (**G**–**I**) and Adriamycin nephropathy (**J** and **L**) mouse models. In contrast to the WT (**A**–**C**), nephrin (red) in both injury models was shifted apically away from the GBM (blue). (**M**–**O**) STORM images of WT (**M**), *Cd2ap*-KO (**N**), and Adriamycin-injured (**O**) glomeruli show an apical shift in podocin staining (red) away from the GBM (blue). (**P**–**R**) STORM images of WT (**P**), *Cd2ap*-KO (**Q**), and Adriamycin-injured (**R**) glomeruli show localization of CD2AP clusters (red) relative to agrin (blue). Note the lack of CD2AP staining in *Cd2ap*-KO (**Q**). Scale bars: 2,000 nm (**A**–**C** and **G**–**L**) and 200 nm (**D**–**F** and **M**–**R**). Ca, capillary; Po, podocyte.

biological studies have suggested that foot process proteins such as podocin, CD2AP, synaptopodin, and α-actinin-4 are components of the slit diaphragm and function by anchoring it to or modifying the cytoskeleton (38). Antibodies against podocin and CD2AP stained in focal clusters in a position that was near the GBM but distinct from the nephrin ectodomain clusters (Figure 3, M and P, respectively; these images are consistent with the ones shown in Figure 1, B and C. CD2AP and podocin therefore localized, as expected, within the foot processes at slit diaphragms, consistent with their proposed roles in anchoring the slit diaphragm.

After FPE, podocin clusters were reduced in size and mostly displaced away from the GBM in all 3 models (Figure 3, N and O, and Supplemental Figure 5). In contrast, CD2AP staining appeared more continuous and was located adjacent to the GBM in the Adriamycin and *Lamb2*-KO models (Figure 3R and Supplemental Figure 6, A and C–F). No CD2AP staining was observed in *Cd2ap*-KO kidney, confirming the specificity of the antibody (Figure 3Q and Supplemental Figure 6B). Interestingly, agrin staining in the *Lamb2*-KO glomeruli was altered, as agrin in the subepithelial aspect of the GBM (the podocyte side) was lost, but it was retained on the inner portion of the GBM (Supplemental Figure 6E). This was specific to the *Lamb2*-KO model, as we did not observe changes in the localization of agrin in the *Cd2ap*-KO or Adriamycin-treated mice (Supplemental Figure 7). Integrin β1, a known receptor for agrin (and laminin-521), could still be detected basally on podocytes (Supplemental Figure 6, F and G).

Synaptopodin redistribution after FPE. To study changes in the actin cytoskeleton after FPE, we examined the distribution of synaptopodin and α-actinin-4 after podocyte injury using STORM. To our surprise, we were still able to see individual synaptopodin clusters (Figure 4, A–F) and α-actinin-4 clusters that matched the pattern of synaptopodin staining (Supplemental Figure 8) adjacent to the GBM. Most of these clusters, however, appeared to be thicker and closer to the GBM than in healthy glomeruli (Figure 4B). We verified that these podocytes were injured using STORM-EM correlation, which showed that the synaptopodin and α-actinin-4 clusters were indeed within areas of FPE (Figure 4, G and H, and Supplemental Figure 9). One obvious change that was consistent in all 3 injury models was the loss of apical synaptopodin from the periphery of podocyte cell bodies (arrowheads in Supplemental Figure 10). The size of synaptopodin clusters adjacent to

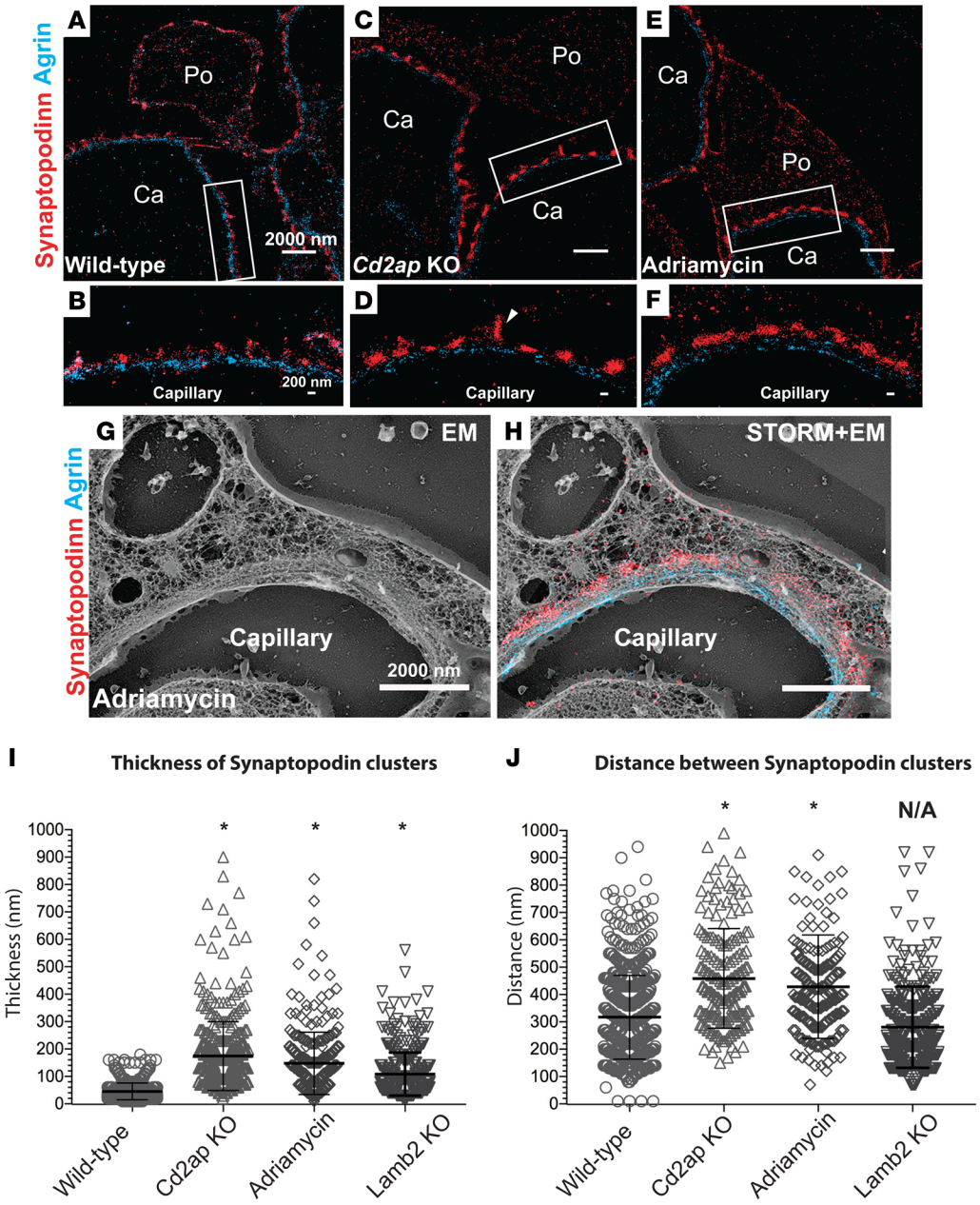

Figure 4. Spatial distribution of synaptopodin after podocyte injury. (**A**–**F**) Double-color STORM imaging of WT (**A** and **B**), *Cd2ap*-KO (**C** and **D**), and Adriamycin-injured (**E** and **F**) glomeruli stained for synaptopodin (red) and agrin (blue). In both injury models, synaptopodin was found in large clusters, closer to the glomerular basement membrane (GBM) than in WT kidneys. Note the single perpendicular synaptopodin cluster in the *Cd2ap*-KO glomerulus (arrowhead in **D**). (**G** and **H**) EM and STORM-EM correlative images, respectively, show that the area imaged is effaced. (**I**) Dot blot showing the sizes of synaptopodin clusters in the 4 models used for this study shows significant increases in the thickness of the clusters upon injury (*$P < 0.00005$ for all the genotypes by Student's *t* test; the experiments and measurements were repeated 2 times). (**J**) Dot blot showing the distances between the adjacent synaptopodin clusters (edge to edge) shows significant increases in the *Cd2ap*-KO and in Adriamycin-induced nephropathy (*$P < 0.00005$ by Student's *t* test) but not in the *Lamb2*-KO (the experiments and measurements were repeated 2 times). Scale bars: 2,000 nm (**A**, **C**, **E**, **G**, and **H**) and 200 nm (**B**, **D**, and **F**). Ca, capillary; Po, podocyte.

the GBM was normally around 35 nm. In contrast, all 3 injury models showed a significant increase in the total thickness of synaptopodin clusters after injury (Figure 4I; *Cd2ap*-KO = 180 nm, Adriamycin = 180 nm, and *Lamb2*-KO = 95 nm). Moreover, the distance between adjacent synaptopodin clusters also showed significant increases in the *Cd2ap*-KO and in Adriamycin-induced nephropathy, but not in the *Lamb2*-KO (WT ~300 nm, *Cd2ap*-KO ~450 nm, Adriamycin ~400 nm, and *Lamb2*-KO ~280 nm).

To determine the fate of contractile actin fibers after FPE, we imaged the 3 podocyte injury models for synaptopodin and myosin IIA by STORM. For *Cd2ap*-KO (Figure 5, A–D), Adriamycin nephropathy (Figure 5, E–H), and *Lamb2*-KO (Supplemental Figure 11), myosin IIA and synaptopodin clusters retained their alternating pattern but were translocated to a position adjacent to the GBM and formed what appeared to be sarcomere-like structures. Confirming that this was specific, we obtained essentially identical results using a second antibody against myosin IIA (Supplemental Figure 12). To determine the percentage of the capillary wall covered with these sarcomere-like structures, we measured the total length of the imaged capillary walls and identified all stretches containing sarcomere-like structures (i.e., alternating synaptopodin and myosin IIA staining) (Figure 5I). In the WT, we observed some stretches with the pattern

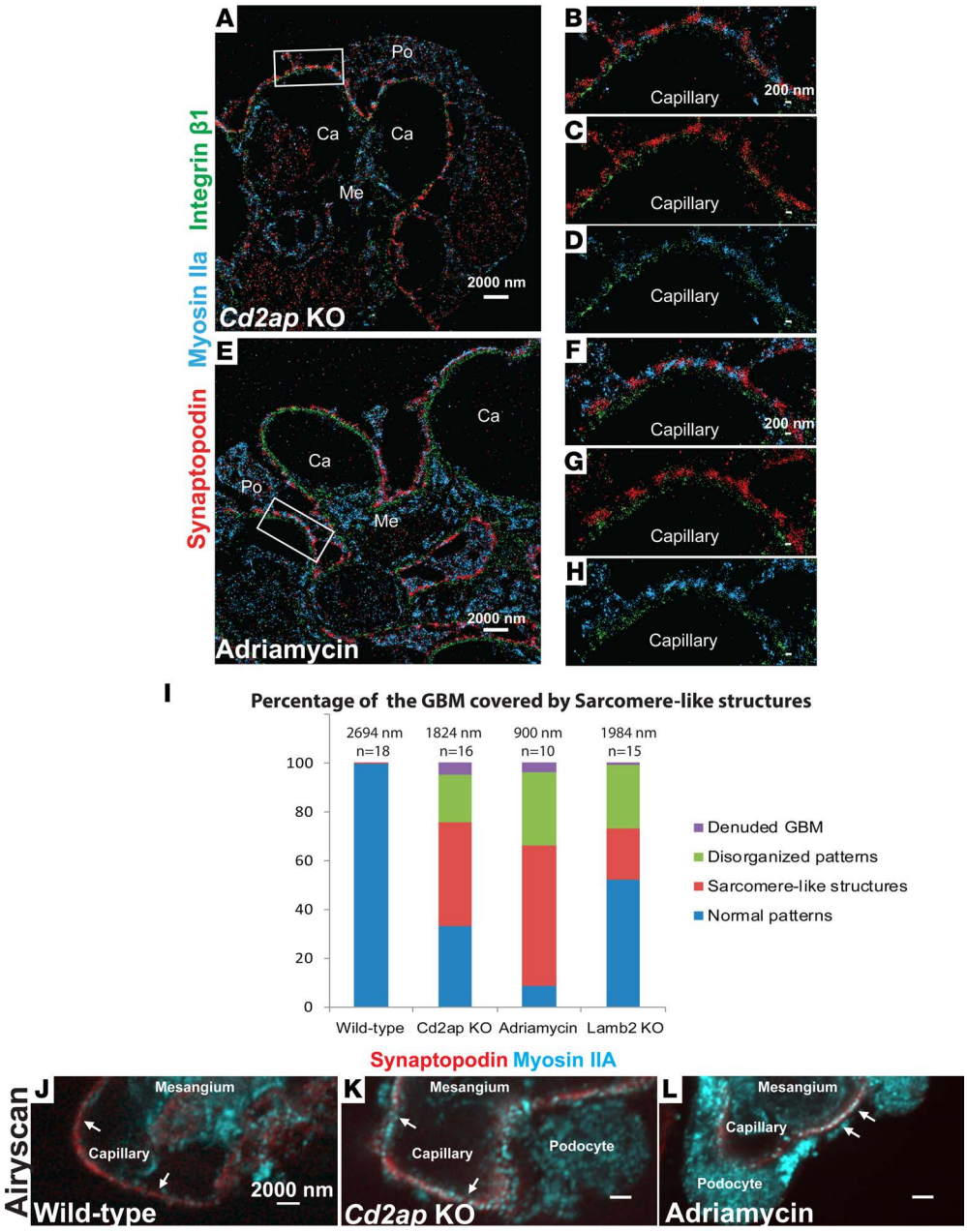

Figure 5. Contractile actin cables in injured podocytes. Triple-color STORM overview images of *Cd2ap*-KO (**A**) and Adriamycin-treated (**E**) glomeruli show myosin IIA's (blue) distribution in comparison with synaptopodin (red) and integrin β1 (green). (**B**–**D** and **F**–**H**) Higher magnification images of the boxed areas in **A** and **E** show the presence of myosin IIA near the glomerular basement membrane (GBM) in both *Cd2ap*-KO (**B**–**D**) and Adriamycin-injured podocytes (**F**–**H**) in sarcomere-like structures. (**I**) Quantification of the percentage of the GBM covered by sarcomere-like structures shows an increase in all injury models over WT. (**J**–**L**) Membrane-extracted isolated glomeruli stained for myosin IIA (blue) and synaptopodin (red) were imaged using Airyscan confocal microscopy to show the capillary wall of the WT (**J**), *Cd2ap*-KO (**K**), and Adriamycin-induced injury (**L**) models. While the WT did not show myosin IIA at the capillary wall (arrows in **J**), alternating clusters of synaptopodin and myosin IIA were apparent in *Cd2ap*-KO and Adriamycin nephropathy (arrows in **K** and **L**, respectively). Scale bars: 2,000 nm (**A**, **E**, and **J**–**L**) and 200 nm (**B**–**D** and **F**–**H**). Ca, capillary; Me, mesangial cell; Po, podocyte.

of sarcomere-like structures, yet those covered less than 0.5% of the length assayed. In contrast, sarcomere-like structures covered 54%, 61%, and 30% of the capillary wall in *Cd2ap*-KO, Adriamycin-treated, and *Lamb2*-KO mice, respectively (Figure 5I). In many segments there was an abundance of myosin IIA present near the GBM in very disorganized or continuous patterns that did not fit the criteria of sarcomere-like structures; these were excluded from the analysis (Supplemental Figure 13).

Our ability to image the actin cytoskeleton of whole glomeruli in situ allowed us to image and reconstruct the 3D layout of podocyte foot processes in super-resolution mode using various antibody combinations. We applied the super-resolution method of Airyscan confocal microscopy, which utilizes a specialized detector to improve the resolution of traditional confocal microscopy without requiring narrowing of the pinhole (39). Traditional confocal microscopy of the whole glomerular surface showed that the myosin IIA–positive actin cables were still present after podocyte injury (Supplemental Figure 14, A–C). Using the Airyscan mode, in WT glomeruli the noncontractile cables (synaptopodin- and phalloidin-positive) were localized mostly adjacent to the capillary wall, while the thicker myosin IIA–positive contractile actin cables were localized away from the capillary wall, in a position consistent with the podocyte cell body

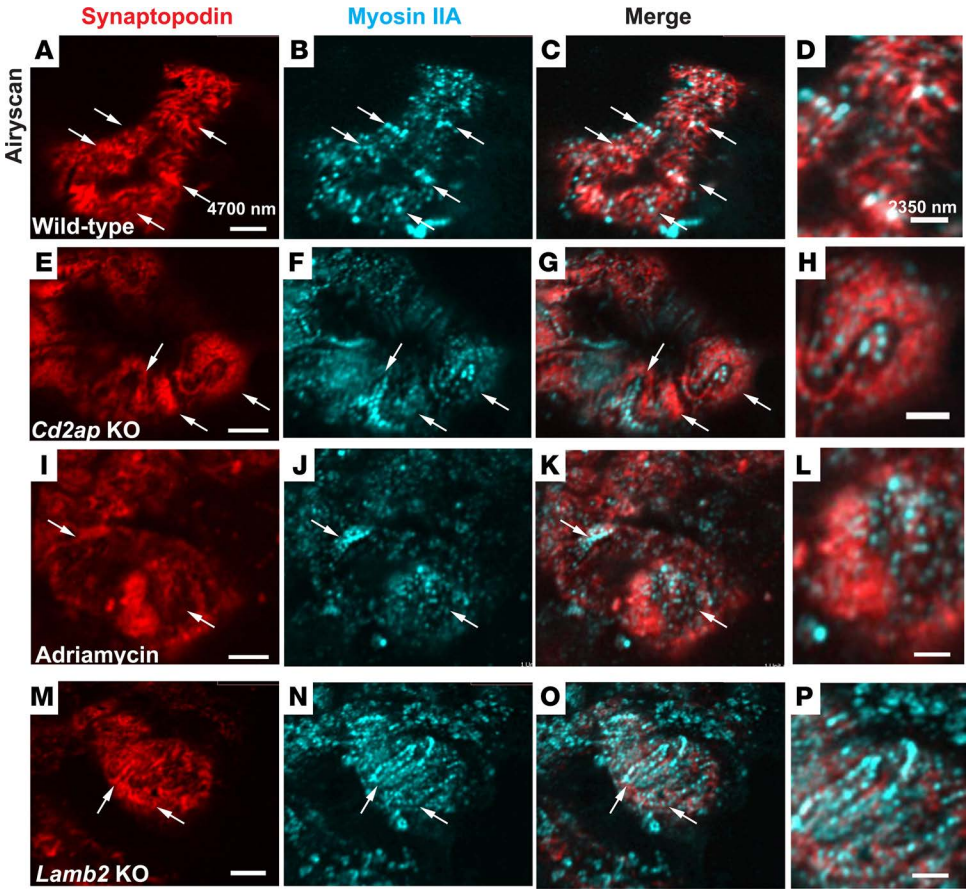

Figure 6. Direct en face imaging of podocyte foot processes. En face views of the capillary wall of decapsulated glomeruli from WT (**A**–**D**), *Cd2ap*-KO (**E**–**H**), Adriamycin-induced injury (**I**–**L**), and *Lamb2*-KO (**M**–**P**) models stained for synaptopodin (red in **A**, **E**, **I**, and **M**) and myosin IIA (blue in **B**, **F**, **J**, and **N**). (**A**–**D**) Healthy podocyte foot processes are synaptopodin-positive (**A** and **C**) and myosin IIA–negative (**B** and **C**); myosin IIA–negative cables branch out of myosin IIA–positive cables (arrows and **D**). (**E**–**P**) Surface views of podocytes with foot process effacement show large synaptopodin-positive areas of effacement (arrows) that stain positive for myosin IIA. Scale bars: 4,700 nm (left 3 columns) and 2,350 nm (fourth column).

(Figure 5J). Single Airyscan confocal slices of the podocyte injury models confirmed that myosin IIA was present in sarcomere-like structures adjacent to the GBM in effaced areas (Figure 5, K and L, and Supplemental Figure 15), which was in contrast to the control (Figure 5J). Collectively, these data demonstrate that there is an extensive floating contractile actin network in podocytes that collapses after injury, falling to a position adjacent to the GBM.

FPE leaves a mat of contractile cables on the basal aspect of podocytes. One advantage of in situ glomerular super-resolution imaging using the Airyscan mode is the ability to directly view whole glomeruli stained with combinations of different antibodies. Taking advantage of this, we costained with antibodies against synaptopodin and myosin IIA to identify the different types of actin cables. In the WT we could resolve the foot processes, which contained synaptopodin but not myosin IIA (Figure 6, A–D); instead, myosin IIA was detected in multiple distinct linear structures that were distal to the GBM (arrows in Figure 6, A–C). Optical sectioning through the glomerulus (Supplemental Movie 1) confirmed distinct localizations of synaptopodin and myosin IIA: synaptopodin was adjacent to the GBM, while myosin IIA was within the podocyte cell body and major processes, confirming our STORM data (Figure 2, A–C). Besides the podocytes, the Z-stack views also showed abundant myosin IIA present in glomerular endothelial and mesangial cells.

In contrast, en face views of injured glomeruli from *Cd2ap*-KO (Figure 6, E–H), Adriamycin-injected (Figure 6, I–L), and *Lamb2*-KO (Figure 6, M–P) mice showed an obvious change in synaptopodin: its localization broadened, and it was no longer visible in the discrete fingerlike patterns observed in controls. In those same areas, myosin IIA sometimes appeared intertwined with synaptopodin in an alternating fashion (arrows in Figure 6, E–G, I–K, and M–O). Moreover, Z-stack views of whole glomeruli from the *Cd2ap*-KO (Supplemental Movie 2), Adriamycin (Supplemental Movie 3), and *Lamb2*-KO (Supplemental Movie 4) injury models showed clearly how synaptopodin and myosin IIA covered the capillary wall in sarcomere-like structures that were not observed in normal podocytes, confirming the STORM data.

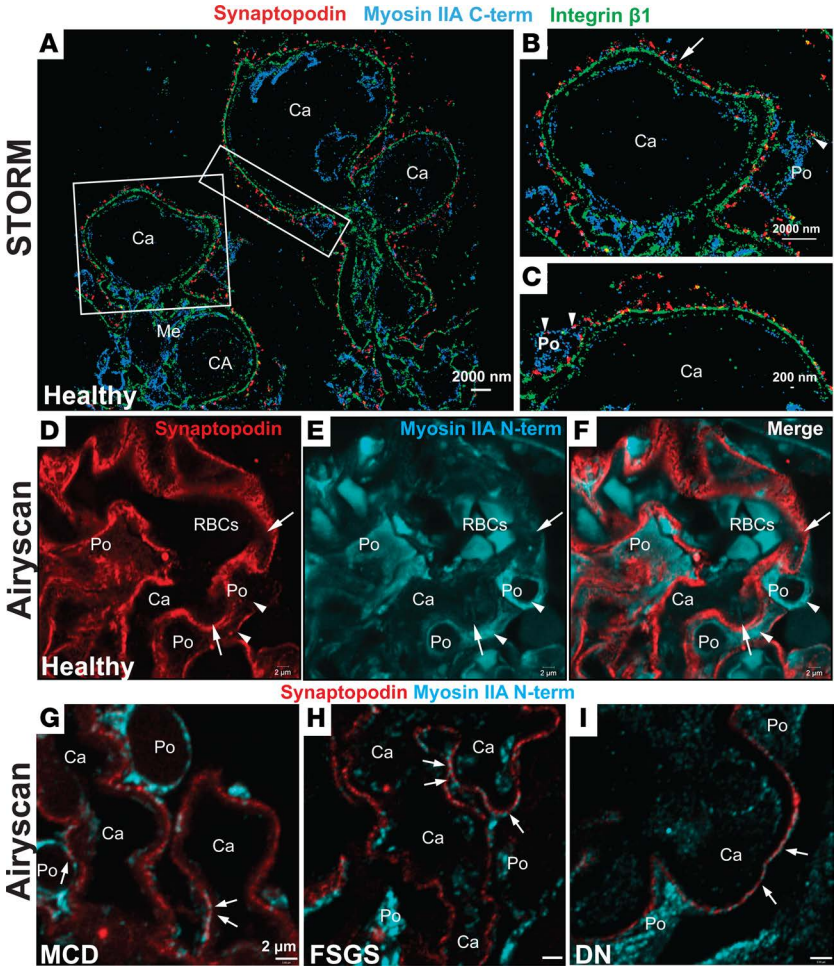

Figure 7. Myosin IIA is present in the human podocyte cell body and major processes but not in foot processes. (**A**–**C**) Triple-color STORM images of a healthy human glomerulus stained for integrin β1 (green), synaptopodin (red), and myosin IIA (blue) show that while podocyte foot processes are labeled by synaptopodin (arrow in **B**), myosin IIA is primarily localized in the podocyte cell body and major processes (arrowheads in **B** and **C**). (**D**–**F**) A healthy human glomerulus stained for synaptopodin (red) and myosin IIA (blue) was imaged by Airyscan super-resolution microscopy. A capillary loop is covered by synaptopodin-positive processes (**D**) that are negative for myosin IIA (**E**) and (**F**). Myosin IIA is present in the podocyte cell body and the major processes (arrowheads), but very little myosin IIA staining overlaps with the finger-like synaptopodin staining (arrows). (**G**–**I**) Airyscan images of human kidney biopsies from patients with minimal change disease (**G**), focal segmental glomerulosclerosis (**H**), and diabetic nephropathy (**I**) labeled with antibodies against synaptopodin (red) and myosin IIA (blue) show the presence of sarcomere-like structures in injured podocytes (arrowheads). Scale bars: 2,000 nm (**A**, **B**, and **D**–**I**) and 200 nm (**C**). Po, podocyte; Ca, capillary; Me, mesangial cell; RBCs, red blood cells; MCD, minimal change disease; FSGS, focal segmental glomerulosclerosis; DN, diabetic nephropathy.

The actin cytoskeleton in human podocytes. Next we investigated the localization of contractile and noncontractile actin filaments in human podocytes using STORM. We stained sections of healthy human glomeruli with synaptopodin, myosin IIA, and integrin β1 antibodies (Figure 7, A–C, and Supplemental Figure 16). The majority of synaptopodin and myosin IIA was localized in a pattern similar to what we found in mouse podocytes. The results of Airyscan imaging were also consistent with those obtained from mouse: synaptopodin was present in areas adjacent to the capillary wall, while myosin IIA was mainly localized away from the capillary wall, in some cases decorating linear actin cables (Figure 7, D–F, and Supplemental Movie 5). Furthermore, based on The Human Protein Atlas (http://www.proteinatlas.org/), which shows that myosin regulatory light chain 2 (MRCL2) is the active light chain of myosin IIA in human podocytes, we used an antibody against MRCL2 and found that, like the myosin IIA heavy chain, MRCL2 was present in podocyte cell bodies and major processes, but not in foot processes (Supplemental Figure 17). This supports the idea that in human podocytes, foot processes normally contain noncontractile actin cables, while the major processes contain myosin IIA–positive contractile cables.

Sarcomere-like structures are features of human podocyte injuries. Since we were able to observe similar distributions of myosin IIA in healthy mouse and human podocytes, we wondered whether human proteinuric diseases that affect podocyte architecture were associated with changes in the spatial distribution of myosin IIA, similar to the nephrotic mouse models. Using both confocal and Airyscan microscopy, we assessed the distribution of synaptopodin and myosin IIA in standard paraffin sections of kidney biopsies from patients diagnosed with minimal change disease (MCD), focal segmental glomerulosclerosis (FSGS), and diabetic nephropathy (DN). In all 3 diseases we could identify areas with distinct sarcomere-like structures (Figure 7, G–I, Supplemental Figures 18 and 19, and Supplemental Movies 6–8). Interestingly, glomerular capillary wall stretches containing podocytes with sarcomere-like structures were much more distinct in the FSGS biopsies than in those from patients with the other 2 diagnoses (Figure 7H and Supplemental Figure 18, E–H).

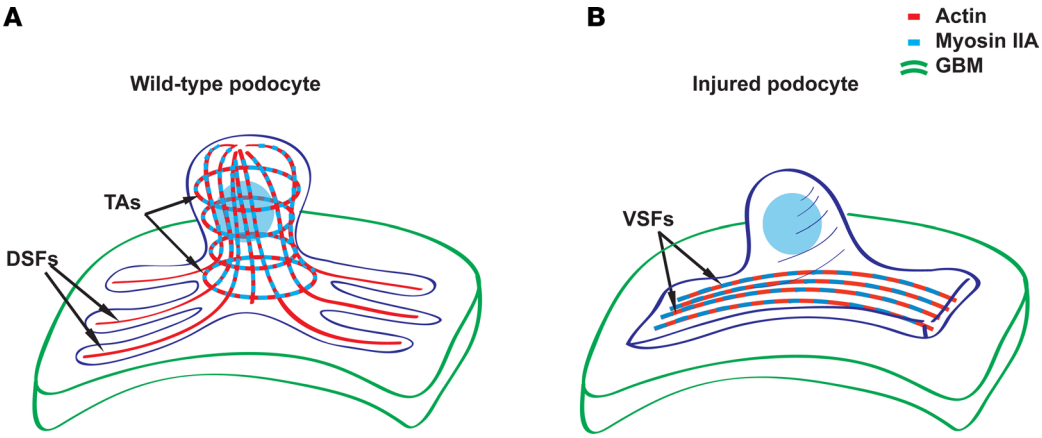

Figure 8. Model of the location of actin cables in podocytes before and after injury. (**A**) WT healthy podocytes contain noncontractile actin cables in the foot processes (analogous to the dorsal stress fibers [DSFs]), and these are connected to the contractile actin cables located in the major processes and the cell body (analogous to the transverse arcs [TAs]). (**B**) Podocyte injury leads to the disassembly of the DSFs in the foot processes that support the contractile actin cables in the TAs, subsequently leading to the appearance of the sarcomere-like contractile actin cables (analogous to the ventral stress fibers [VSFs]) juxtaposed to the glomerular basement membrane (GBM).

Discussion

Here we have imaged for the first time to our knowledge at super-resolution the organization of the actin cytoskeleton in the context of a complex, multicellular structure, the glomerulus. Blood flows through these capillaries at some of the highest capillary pressures in the body, allowing the porous but permselective walls of the capillary to filter away water, solutes, and small proteins. The ability of fluid and solutes to pass across the podocytes' interdigitated foot processes is mediated by the porous slit diaphragms that bridge the space between them (40).

The actin cytoskeleton is thought to play a critical role in establishing and maintaining the podocyte's unique cellular architecture for several reasons. First, the complex morphology of the podocyte contains diverse actin structures, including thick actin cables in both the major and the foot processes, and more diffuse branched actin networks in the foot processes. Second, it is thought that tight adhesion to the GBM is critical to allow podocytes to maintain their positions in the face of the hydrostatic forces pushing them away from the capillary wall. Integrins bound to the GBM are anchored to the actin cytoskeleton through a variety of actin- and integrin-binding proteins to form structures that are likely analogous to the focal adhesions characterized in cell culture.

Our work demonstrates that the thick actin cables in the major processes contain myosin IIA and α-actinin-4 in an alternating fashion and are therefore, by definition, contractile actin fibers, while the actin cables in the foot processes lacking myosin IIA are therefore noncontractile. Our data are consistent with 2 recent reports indicating that myosin IIA might be in the major processes but not in the foot processes (18, 19). This suggests a system in which the contractile forces distal to the capillary wall generate tension by pulling the noncontractile actin fibers anchored to adhesion complexes at the GBM and to the slit diaphragms that link adjacent foot processes. Tension pulling on integrin complexes both induces the assembly of and reinforces focal adhesion complexes that link integrins to the actin cytoskeleton (41). Slit diaphragm proteins also likely require tension to maintain the spaces for efficient filtration between foot processes. We speculate that the link between these 3 components (i.e., the noncontractile actin cables, the integrin-based adhesion complexes, and the slit diaphragm) and the pulling force applied on these structures play a critical role in maintaining podocyte adhesion and function.

This system of distal contractile actin filaments pulling against noncontractile filaments at the base of the podocyte is surprising given that the hydrostatic force is pushing the cell in the same direction as the contractive force. But it is consistent with the model of floating compression known as tensegrity (42). Tensegrity, a concept first popularized by Buckminster Fuller, demonstrates that complex structures can be maintained by a system of continuous tension (43). Ingber and associates have adapted the concept of tensegrity to biological structures such as the musculoskeletal and cytoskeletal systems (44–47). Tensegrity structures generate strength by using continuous tension to distribute forces across a large number of

structural elements. One advantageous feature of tensegrity is formation of structures that are resilient to compressive forces. Tensegrity requires elements that generate tension and others that resist compression. In biological systems, tension can be generated by contractile actin fibers, while compressive forces can be resisted by extracellular adhesions and microtubules (45).

While tensegrity structures are resistant to collapse from the failure of any single component, loss of tension would result in complete structural collapse. Our previous work demonstrated that activation of the small GTPase Rac results in FPE (48). Rac activation reduces cell tension by antagonizing Rho, a major regulator of myosin II activity (49). Thus, the tensegrity model predicts that Rac activation induced by podocyte injury would result in loss of cellular tension and a collapse of the cytoskeletal network, with the large contractile filaments becoming localized to the bottom of the cell juxtaposed to the GBM.

Super-resolution imaging allowed us to identify sarcomere-like myosin-containing fibers in the podocyte cell body and major processes (Figure 8A). We observed alternating myosin and α-actinin stripes in both the proximal actin cables and in the actin mat at the base of podocytes after FPE (Figure 8B). Moreover, the use of Airyscan confocal microscopy on isolated glomeruli provided views of the whole glomerular structure in super-resolution mode. This 1.7-fold improvement in resolution by using the Airyscan detectors was enough to resolve individual podocyte foot processes (39). Importantly, the use of Airyscan allowed us to overcome the limitation of STORM's total internal reflection fluorescence optical design that only images structures within 150 nm of the glass. We suspect that our methods will be generally applicable to the analysis of tissue-specific actin structures in other tissues.

Our super-resolution imaging indicates that FPE caused by different modes of podocyte injury coincides with the redistribution of myosin IIA towards the GBM, in an alternating pattern with α-actinin-4, to form sarcomere-like structures (Figure 8B). This is reminiscent of the actin mat described as part of FPE in both animal models and human glomerular diseases (23, 50). Our data suggest that myosin IIA redistribution after podocyte injury is one of the molecular changes that lead to FPE, opening the door for more mechanistic studies of this process and how it can be reversed. However, whether the altered contractile fiber distribution is a cause or an effect of FPE remains to be determined.

As in cultured cells (13, 14), our work suggests that the actin fibers in the foot processes are similar to the noncontractile DSFs, while the contractile fibers in the major processes as well as in the outer, apical membranes are similar to TAs that place the DSFs under tension. We did not identify any contractile filaments on the basal surface that could correspond to VSFs in uninjured podocytes. However, it is thought that at least a portion of the VSFs seen in vitro may correspond to TAs that have moved progressively from the apical to the basal surface (32). Their presence as VSFs could represent a tissue culture artifact or a cell-type-specific actin fiber. Our work, to our knowledge, represents the first demonstration of DSFs and TAs in vivo.

Synaptopodin was recently shown to be mechanoresponsive, as it localizes to cell-cell adhesions in a tension-dependent manner (30). In vitro, synaptopodin recruits α-actinin-4 to cell-cell adhesions, leading to adhesion strengthening and epithelial barrier formation (30). In vivo, STORM showed that synaptopodin and α-actinin-4 colocalized on basal actin filaments both in healthy and in injured podocytes after FPE. We therefore speculate that both noncontractile and contractile actin cables are under tension in podocytes in vivo.

The tensegrity model predicts that the recovery of podocyte integrity after FPE will require both oriented myosin-mediated tension and potentially the formation of short microtubule clusters that would help lift the podocyte cell body away from the GBM as foot processes reform. The new concepts developed from these studies help us to not only understand the events underlying podocyte collapse, but can also help us to understand how homeostasis can be restored.

Methods

Reagents and mice. Previously described *Cd2ap*-KO (35) and *Lamb2*-KO (36, 51) mice and their littermate controls were used at 2.5 weeks of age. Adriamycin nephropathy was induced in BALB/cJ mice (The Jackson Laboratory) at 12 weeks of age as previously reported (37). In brief, male mice weighing 20 to 25 g were injected once in the tail vein with 14 mg/kg body weight of Adriamycin (doxorubicin hydrochloride; Sigma-Aldrich, D1515). Mice were monitored for proteinuria and sacrificed at day 9 after injection.

Tissue processing for STORM imaging. Tissue preservation was performed as reported previously (27). In brief, kidneys were isolated after transcardial perfusion with phosphate-buffered saline (PBS) containing 4% paraformaldehyde (PFA; Electron Microscopy Sciences). After dissection, kidneys were cut into smaller

pieces and fixed further for 4 hours in 4% PFA in PBS. The samples were then washed with PBS multiple times before immersion in a cryoprotectant solution of 2.3 M sucrose plus 10% polyvinylpyrrolidone (PVP) in 0.1 M PIPES (pH = 7.2) overnight at 4°C. Cryoprotected tissues were mounted on a metal sectioning pin and frozen by immersion in liquid nitrogen.

Glomerular isolation and detergent extraction. Glomeruli were isolated by perfusing mice with Dynabeads as previously described (52) but without collagenase digestion. Glomeruli were then subjected to membrane extraction as previously described (53). Throughout the different steps a magnet was used to prevent loss of glomeruli during washes. The extraction buffers (KHMgE buffers) contained 10 μM phalloidin, 10 μM taxol, 2 mM ATP, 1 mM phenylmethylsulfonyl fluoride, 10 μM leupeptin in 0.1 M KCl, 30 mM HEPES at pH 7.2, 10 mM $MgCI_2$, and 2 mM EGTA at pH 7.1. Two types of extraction solutions were used: solution A used for the ultrastructural studies contained 0.01% saponin and 0.5% Triton X-100; solution B used for confocal microscope studies contained 0.01% saponin and 0.05% Triton X-100. Before the extraction procedure, samples were preincubated with the KHMgE solution for 1.5 minutes, and then detergent extracted for 1.5 minutes in the respective extraction solution before fixing the sample for 10 minutes in 4% PFA in the presence of 0.01% saponin and 0.5% Triton X-100.

For immunofluorescence, detergent-extracted glomeruli were fixed in 4% PFA for 10 minutes and then washed 3 times with KHMgE before switching to PBS. The glomeruli were then washed once with 50 mM glycine in PBS for 10 minutes and blocked with 2% bovine serum albumin (BSA) for 2 hours at 4°C before applying the primary antibody mix in 2% BSA overnight at 4°C. Samples were then washed 3 times with PBS before applying secondary antibodies for 45 minutes at room temperature. Samples were washed twice in PBS for 10 minutes each, and then phalloidin plus DAPI staining was performed for 10 minutes before fixing the samples in 3% PFA and 0.05% glutaraldehyde for 10 minutes. Samples were mounted on a slide and prepared for confocal microscopy.

Human tissue samples. Five different deidentified formalin-fixed, paraffin-embedded (FFPE) histologically normal human kidney samples were provided by the Washington University Division of Nephrology's Kidney Translational Research Core (KTRC). After deparaffinization, samples were antigen retrieved overnight at 65°C in TE buffer (10 mM EDTA, 1 mM Tris-base, pH 9.0) and then processed for immunohistochemistry as described below. Samples were imaged by Airyscan using the Z-stack function, and 3D composite images were processed using Volocity software (PerkinElmer). For studies of diseased kidneys, 6 biopsies of MCD, FSGS, and DN FFPE kidney were used.

Antibodies and immunohistochemistry for STORM imaging. Frozen tissues were sectioned at approximately 200 nm on a Leica EM-FC6 ultracryomicrotome equipped with a diamond knife, and sections were collected on carbon-coated coverslips. Sections were refixed for 20 minutes at room temperature with 4% PFA, followed by 3 washes in PBS; excess PFA was quenched using 50 mM glycine in PBS. Sections were further processed for immunolabeling in the following manner: (a) blocked overnight at 4°C using 2% BSA in PBS, (b) incubated with primary antibodies diluted in 2% BSA in PBS overnight at 4°C, (c) washed in PBS 3 × 20 minutes at room temperature, (d) incubated with secondary antibodies diluted in 2% BSA in PBS at room temperature for 2–3 hours, and (e) washed in PBS at room temperature. Immunolabeled sections were postfixed using 3% PFA plus 0.05% glutaraldehyde in PBS, washed in PBS, and visualized by STORM.

The primary antibodies were nephrin extracellular domain (R&D Systems, AF3159, goat anti-mouse, 1:750), podocin (IBL International, JP29040, rabbit anti-human, 1:500), CD2AP (rabbit anti-mouse, 1:5,000) (35), synaptopodin (Synaptic Systems, 163004, guinea pig anti-mouse, 1:1,500), synaptopodin (Millipore, ABN481, rabbit anti–human COOH-terminus, 1:500), α-actinin-4 (gift from Martin Pollak [Beth Israel-Deaconess Medical Center, Boston, Massachusetts, USA]; rabbit anti–human NH_2-terminus, 1:1,500) (54), myosin IIA Poly19098 (Covance, PRB-440P, rabbit anti-human, 1:1,500), myosin IIA (gift from Paul Bridgman [Washington University School of Medicine], rabbit anti–human COOH-terminus, 1:1,500) (55, 56), myosin IIA (Abnova, clone 3C7, mouse anti–human NH_2-terminus, 1:500), MRLC2 (Assay BioTech, B0690, rabbit anti-human, 1:500), agrin (rabbit anti-mouse, 1:15,000 or hamster anti-mouse, 1:2,000) (57), and integrin β1 (BD Pharmingen, clone 9EG7, 553715, rat anti-mouse, 1:500). Alexa Fluor 555 Phalloidin (Thermo Fisher Scientific, A34055) was used at 1:500. Secondary antibodies for STORM were purchased from Jackson ImmunoResearch Laboratories and custom conjugated to Alexa647 reporter dye and either Alexa405, Cy2, or Cy3 activator dyes as described previously (58).

Confocal Airyscan microscope imaging. Isolated glomeruli were imaged on an LSM880 Zeiss equipped with the Airyscan mode or on an Olympus FV1000 confocal microscope using the Z-stack function. Confocal

optical sectioning (0.25 μm thick) was used to image individual glomeruli. Z-stacks were processed using Volocity and Imaris (Oxford Instruments) software, and single optical sections were chosen as representative images. From each genotype, 10 encapsulated and 10 decapsulated glomeruli were imaged.

STORM imaging. STORM setup and image acquisition schemes were similar to those described before (59) with the following modifications. Illumination lasers were 642 nm (Vortran), 561 nm, 488 nm (Coherent, Sapphire), and 405 nm (Coherent, Cube). In all experiments described here, we performed single-reporter (Alexa647) multiple-activator STORM as described earlier (27, 60). Alexa647 images (~10,000 images per channel) acquired by the same objective were separated using a quad band dichroic ZT405/488/561/640rpc and filtered using an ET705/72m emission filter (Chroma). Images were captured on an EM-CCD camera (iXon+ DU897, Andor) and analyzed using custom software. Image stacks were fitted with an elliptical Gaussian function to determine the centroid positions of fluorescent pixel intensity peaks. These positions termed "STORM localizations" were rendered as STORM images or analyzed further quantitatively.

N-STORM analysis. For quantification, STORM images were obtained using the Nikon N-STORM according to the manufacturer's instructions. For comparison reasons, fixed laser power and number of frames were collected from all the genotypes used in this study. After normalization using the same parameters, N-STORM images were analyzed using the NIS-Elements AR software, V4.50. Synaptopodin cluster thickness was evaluated by measuring the average area of synaptopodin clusters adjacent to the GBM in multichannel STORM images. The distance between individual synaptopodin clusters was determined by measuring the average distance between the edges of the adjacent clusters. To evaluate the length of the sarcomere-like structures in injured glomeruli, the whole length of the GBM in ultrathin sections was determined, and then the areas covered by sarcomere-like structures were measured and represented as percentages of the total capillary loop length.

Quick-freeze deep-etch fracture and electron microscopy. For STORM-EM correlation, after STORM imaging the nail polish from the coverglass was carefully removed by immersing in PBS. The tissue sections were fixed in 2% glutaraldehyde in 100 mM NaCl, 30 mM HEPES, and 2 mM $CaCl_2$, pH 7.2 (NaHCaCl) at room temperature. Areas (3 × 3 mm) of the coverglass containing STORM-imaged sections were cut, rinsed in dH_2O, and frozen by abrupt application of the sample against a liquid helium–cooled copper block with a Cryopress freezing machine. Frozen samples were transferred to a liquid nitrogen–cooled Balzers 400 vacuum evaporator, etched for 20 minutes at −80°C, and rotary replicated with approximately 2-nm platinum deposited from a 20° angle above the horizontal, followed by an immediate, approximately 10-nm stabilization film of pure carbon deposited from an 85° angle. Replicas were floated onto a dish of concentrated hydrofluoric acid and transferred through several rinses of dH_20 with a loopful of Photo-flo, picked up on Luxel grids (LUXEL), and photographed on a JEOL 1400 microscope with attached AMT digital camera. The glomeruli imaged by EM were matched with the corresponding STORM images, and the 2 images were superimposed using Adobe Photoshop.

Statistics. *P* values in Figure 4, I and J were calculated using a 2-tailed Student's *t* test using accumulated data from 2 independent experiments. The number of glomeruli (*n*) used for the statistical analysis (Figures 4 and 5) from the WT, *Cd2ap*-KO, Adriamycin, and *Lamb2*-KO mice were 18, 16, 10, and 15 glomeruli, respectively.

Study approval. Animal studies were approved by the Washington University Institutional Animal Care and Use Committee. Human kidney samples were procured from patients who provided written informed consent by the KTRC under a human studies protocol approved by the Washington University Institutional Review Board.

Author contributions

HYS performed the experiments, analyzed the data, and wrote the manuscript. RR performed the deep-etch freeze-fracture for STORM-EM correlation. JEH designed the deep-etch and STORM-EM correlation experiments. SJ provided human kidney sections. JHM and ASS provided mice, participated in data analysis, and wrote and edited the manuscript.

Acknowledgments

We thank Wandy Beatty for her assistance with ultrathin sectioning, Paul Bridgman for the myosin IIA (C-terminus) antibody, Martin Pollak for the α-actinin-4 antibody, and Takako Sasaki for the rabbit antibody against agrin. We thank Diane Salomon in the KTRC for patient enrollments, regulatory approvals, and specimen processing, Robert Grubb and Ramakrishna Venkatesh for assistance with obtaining nephrectomy samples, and

Alma Johnson for assistance with histological sections. The quantitative STORM data were generated and analyzed through the Washington University Center for Cellular Imaging with support from microgrants. This project was supported by NIH grants R01DK058366 (to AS and JM) and R01DK078314 (to JM), by a NephCure Kidney International Young Investigator Award (to HS), by a Career Development Fellowship (to HS) from the Nephrotic Syndrome Study Network Consortium (funded by NIH grant U54DK083912), and by Scientist Development Grant 17SDG33420069 (to HS) from the American Heart Association.

Address correspondence to: Andrey Shaw, Genentech, Research Biology, One DNA Way, MS93B, South San Francisco, California 94080, USA. Phone: 650.225.2367; Email: shaw.andrey@gene.com. Or to: Jeffrey Miner, Washington University School of Medicine, Division of Nephrology, 4523 Clayton Ave., St. Louis, Missouri 63110, USA. Phone: 314.362.8235; Email: minerj@wustl.edu.

1. Gabbiani G, Hirschel BJ, Ryan GB, Statkov PR, Majno G. Granulation tissue as a contractile organ. A study of structure and function. *J Exp Med*. 1972;135(4):719–734.
2. Tomasek JJ, Gabbiani G, Hinz B, Chaponnier C, Brown RA. Myofibroblasts and mechano-regulation of connective tissue remodelling. *Nat Rev Mol Cell Biol*. 2002;3(5):349–363.
3. Fu NY, et al. EGF-mediated induction of Mcl-1 at the switch to lactation is essential for alveolar cell survival. *Nat Cell Biol*. 2015;17(4):365–375.
4. Wong AJ, Pollard TD, Herman IM. Actin filament stress fibers in vascular endothelial cells in vivo. *Science*. 1983;219(4586):867–869.
5. Burridge K, Wittchen ES. The tension mounts: stress fibers as force-generating mechanotransducers. *J Cell Biol*. 2013;200(1):9–19.
6. Kwon O, Phillips CL, Molitoris BA. Ischemia induces alterations in actin filaments in renal vascular smooth muscle cells. *Am J Physiol Renal Physiol*. 2002;282(6):F1012–F1019.
7. Vallenius T. Actin stress fibre subtypes in mesenchymal-migrating cells. *Open Biol*. 2013;3(6):130001.
8. Burridge K. Are stress fibres contractile? *Nature*. 1981;294(5843):691–692.
9. Pelham RJ, Wang Yl. High resolution detection of mechanical forces exerted by locomoting fibroblasts on the substrate. *Mol Biol Cell*. 1999;10(4):935–945.
10. Mitchison TJ, Cramer LP. Actin-based cell motility and cell locomotion. *Cell*. 1996;84(3):371–379.
11. dos Remedios CG, et al. Actin binding proteins: regulation of cytoskeletal microfilaments. *Physiol Rev*. 2003;83(2):433–473.
12. Guillot C, Lecuit T. Mechanics of epithelial tissue homeostasis and morphogenesis. *Science*. 2013;340(6137):1185–1189.
13. Small JV, Rottner K, Kaverina I, Anderson KI. Assembling an actin cytoskeleton for cell attachment and movement. *Biochim Biophys Acta*. 1998;1404(3):271–281.
14. Heath JP. Behaviour and structure of the leading lamella in moving fibroblasts. I. Occurrence and centripetal movement of arc-shaped microfilament bundles beneath the dorsal cell surface. *J Cell Sci*. 1983;60:331–354.
15. Tojkander S, Gateva G, Husain A, Krishnan R, Lappalainen P. Generation of contractile actomyosin bundles depends on mechanosensitive actin filament assembly and disassembly. *Elife*. 2015;4:e06126.
16. Miner JH. The glomerular basement membrane. *Exp Cell Res*. 2012;318(9):973–978.
17. Drenckhahn D, Franke RP. Ultrastructural organization of contractile and cytoskeletal proteins in glomerular podocytes of chicken, rat, and man. *Lab Invest*. 1988;59(5):673–682.
18. Hays T, et al. Proteomics analysis of the non-muscle myosin heavy chain IIa-enriched actin-myosin complex reveals multiple functions within the podocyte. *PLoS One*. 2014;9(6):e100660.
19. Miura K, et al. Podocyte expression of nonmuscle myosin heavy chain-IIA decreases in idiopathic nephrotic syndrome, especially in focal segmental glomerulosclerosis. *Nephrol Dial Transplant*. 2013;28(12):2993–3003.
20. Lim BJ, Yang JW, Do WS, Fogo AB. Pathogenesis of focal segmental glomerulosclerosis. *J Pathol Transl Med*. 2016;50(6):405–410.
21. Kriz W, Shirato I, Nagata M, LeHir M, Lemley KV. The podocyte's response to stress: the enigma of foot process effacement. *Am J Physiol Renal Physiol*. 2013;304(4):F333–F347.
22. D'Agati VD. The spectrum of focal segmental glomerulosclerosis: new insights. *Curr Opin Nephrol Hypertens*. 2008;17(3):271–281.
23. Shirato I. Podocyte process effacement in vivo. *Microsc Res Tech*. 2002;57(4):241–246.
24. Yu H, et al. A role for genetic susceptibility in sporadic focal segmental glomerulosclerosis. *J Clin Invest*. 2016;126(3):1067–1078.
25. Small J, Rottner K, Hahne P, Anderson KI. Visualising the actin cytoskeleton. *Microsc Res Tech*. 1999;47(1):3–17.
26. Huang B, Wang W, Bates M, Zhuang X. Three-dimensional super-resolution imaging by stochastic optical reconstruction microscopy. *Science*. 2008;319(5864):810–813.
27. Suleiman H, et al. Nanoscale protein architecture of the kidney glomerular basement membrane. *Elife*. 2013;2:e01149.
28. Pavenstädt H, Kriz W, Kretzler M. Cell biology of the glomerular podocyte. *Physiol Rev*. 2003;83(1):253–307.
29. Bi J, Chase SE, Pellenz CD, Kurihara H, Fanning AS, Krendel M. Myosin 1e is a component of the glomerular slit diaphragm complex that regulates actin reorganization during cell-cell contact formation in podocytes. *Am J Physiol Renal Physiol*. 2013;305(4):F532–F544.
30. Kannan N, Tang VW. Synaptopodin couples epithelial contractility to α-actinin-4-dependent junction maturation. *J Cell Biol*. 2015;211(2):407–434.
31. Pellegrin S, Mellor H. Actin stress fibres. *J Cell Sci*. 2007;120(Pt 20):3491–3499.
32. Hotulainen P, Lappalainen P. Stress fibers are generated by two distinct actin assembly mechanisms in motile cells. *J Cell Biol*. 2006;173(3):383–394.
33. Burnette DT, et al. A contractile and counterbalancing adhesion system controls the 3D shape of crawling cells. *J Cell Biol*. 2014;205(1):83–96.

34. Johnstone DB, et al. Podocyte-specific deletion of Myh9 encoding nonmuscle myosin heavy chain 2A predisposes mice to glomerulopathy. *Mol Cell Biol*. 2011;31(10):2162–2170.
35. Shih NY, Li J, Cotran R, Mundel P, Miner JH, Shaw AS. CD2AP localizes to the slit diaphragm and binds to nephrin via a novel C-terminal domain. *Am J Pathol*. 2001;159(6):2303–2308.
36. Noakes PG, Miner JH, Gautam M, Cunningham JM, Sanes JR, Merlie JP. The renal glomerulus of mice lacking s-laminin/laminin beta 2: nephrosis despite molecular compensation by laminin beta 1. *Nat Genet*. 1995;10(4):400–406.
37. Wang Y, Wang YP, Tay YC, Harris DC. Progressive Adriamycin nephropathy in mice: sequence of histologic and immunohistochemical events. *Kidney Int*. 2000;58(4):1797–1804.
38. Mundel P, Reiser J. Proteinuria: an enzymatic disease of the podocyte? *Kidney Int*. 2010;77(7):571–580.
39. Huff J. The Airyscan detector from ZEISS: confocal imaging with improved signal-to-noise ratio and super-resolution. *Nat Meth*. 2015;12.
40. Rodewald R, Karnovsky MJ. Porous substructure of the glomerular slit diaphragm in the rat and mouse. *J Cell Biol*. 1974;60(2):423–433.
41. Riveline D, et al. Focal contacts as mechanosensors: externally applied local mechanical force induces growth of focal contacts by an mDia1-dependent and ROCK-independent mechanism. *J Cell Biol*. 2001;153(6):1175–1186.
42. Stamenovic D, Ingber DE. Tensegrity-guided self assembly: from molecules to living cells. *Soft Matter*. 2009;5(6):1137–1145.
43. Fuller B. Tensegrity. *Portfolio Artnews Annual*. 1961;4.
44. Ingber DE. Tensegrity II. How structural networks influence cellular information processing networks. *J Cell Sci*. 2003;116(Pt 8):1397–1408.
45. Ingber DE. Tensegrity I. Cell structure and hierarchical systems biology. *J Cell Sci*. 2003;116(Pt 7):1157–1173.
46. Ingber DE. Cellular tensegrity: defining new rules of biological design that govern the cytoskeleton. *J Cell Sci*. 1993;104(Pt 3):613–627.
47. Chen CS, Ingber DE. Tensegrity and mechanoregulation: from skeleton to cytoskeleton. *Osteoarthr Cartil*. 1999;7(1):81–94.
48. Yu H, et al. Rac1 activation in podocytes induces rapid foot process effacement and proteinuria. *Mol Cell Biol*. 2013;33(23):4755–4764.
49. Burridge K, Wennerberg K. Rho and Rac take center stage. *Cell*. 2004;116(2):167–179.
50. Smoyer WE, Mundel P, Gupta A, Welsh MJ. Podocyte alpha-actinin induction precedes foot process effacement in experimental nephrotic syndrome. *Am J Physiol*. 1997;273(1 Pt 2):F150–F157.
51. Jarad G, Cunningham J, Shaw AS, Miner JH. Proteinuria precedes podocyte abnormalities in$Lamb2^{-/-}$ mice, implicating the glomerular basement membrane as an albumin barrier. *J Clin Invest*. 2006;116(8):2272–2279.
52. Takemoto M, et al. A new method for large scale isolation of kidney glomeruli from mice. *Am J Pathol*. 2002;161(3):799–805.
53. Nakata T, Hirokawa N. Cytoskeletal reorganization of human platelets after stimulation revealed by the quick-freeze deep-etch technique. *J Cell Biol*. 1987;105(4):1771–1780.
54. Kaplan JM, et al. Mutations in ACTN4, encoding alpha-actinin-4, cause familial focal segmental glomerulosclerosis. *Nat Genet*. 2000;24(3):251–256.
55. Rochlin MW, Itoh K, Adelstein RS, Bridgman PC. Localization of myosin II A and B isoforms in cultured neurons. *J Cell Sci*. 1995;108(Pt 12):3661–3670.
56. Phillips CL, Yamakawa K, Adelstein RS. Cloning of the cDNA encoding human nonmuscle myosin heavy chain-B and analysis of human tissues with isoform-specific antibodies. *J Muscle Res Cell Motil*. 1995;16(4):379–389.
57. Harvey SJ, et al. Disruption of glomerular basement membrane charge through podocyte-specific mutation of agrin does not alter glomerular permselectivity. *Am J Pathol*. 2007;171(1):139–152.
58. Bates M, Huang B, Dempsey GT, Zhuang X. Multicolor super-resolution imaging with photo-switchable fluorescent probes. *Science*. 2007;317(5845):1749–1753.
59. Dani A, Huang B, Bergan J, Dulac C, Zhuang X. Superresolution imaging of chemical synapses in the brain. *Neuron*. 2010;68(5):843–856.
60. Huang B, Jones SA, Brandenburg B, Zhuang X. Whole-cell 3D STORM reveals interactions between cellular structures with nanometer-scale resolution. *Nat Methods*. 2008;5(12):1047–1052.